ASIAN
JOURNAL OF PHYSICS

A Special Issue

Dedicated to

Prof Kehar Singh

Formerly Professor of Physics

at IIT Delhi

Guest Editor : R. S. Sirohi

Vectorial imaging techniques for insights into the principles of optical tweezers

Sirshendu Dinda and Debabrata Goswami

Department of Chemistry

Indian Institute of Technology Kanpur-208 016, India.

This article is dedicated to Prof Kehar Singh for his significant contributions to Optics and Photonics

Optical tweezers work on the principle that microscopic particles may be immobilized by the application of an intense photon flux, which may be attained under tight focusing conditions. To elucidate the behaviour and mechanism of this tweezing action, herein we perform numerical studies and investigate the intensity distribution at the focusing spot under tight focusing conditions. With a high numerical aperture optical lens, the influence of the incident beam polarization on the intensity distribution of focusing spot is very significant. A linearly polarized incident beam induces an asymmetric focusing spot, which is elongated along the polarization direction of the incident beam. The incident beam profile influences the shape of the focusing spot. We show here how introducing an optical mask in front of the optical lens can induce many impressive results; e.g., incident beam modulated by an amplitude mask induces a sub-diffraction limit focusing spot which is relevant to further studies on optical tweezers. We also demonstrate the effects of considering interfaces of different numerical apertures in an optical setup. Thus, we report on the multiple aspects of light-matter interactions for high numerical aperture lens setups, wherein we show through simulations and experiments, the characteristics of such systems that are of use to the broader optics community. © Anita Publications. All rights reserved.

Keywords: Vectorial imaging, Intensity distribution patterns, Amplitude masks, Optical tweezers

1 Introduction

High spatial resolution is an essential requirement of imaging microscopes, such as confocal laser scanning microscope, near-field scanning optical microscope, etc. The use of a confocal set-up to generate an optical trap, manipulate trapped particles, and measure physical parameters in trap volume opens new horizons. In all the experiments, where a confocal optical microscopy setup is involved, a precise spatial intensity distribution in the optical volume is necessary to interpret or predict the results accurately.

The spatial resolution of a standard far-field optical microscope is limited to the sub-micrometre scale. This limitation of the optical microscopy resolution is mainly caused by the well-known "diffraction limit", which is the consequence of the wave property of light. In this paper, we discuss the generation of the diffraction-limited focusing spot by a high numerical aperture objective, used in an optical microscope setup.

2 Elementary principle of diffraction

Light waves have three distinct properties, reflection, refraction, and diffraction; all of which are interactions between the light waves and matter under the approximations of classical optics, where no alteration of the material properties occur in such interactions. Reflection involves a change in the direction of propagation of light waves when they bounce off a barrier. The refraction of light waves involves a change in the direction of propagation as well as the change in wavelength as they pass from one medium to another.

Corresponding author :
e-mail: dgoswami@iitk.ac.in (Debabrata Goswami)

Furthermore, diffraction involves a change in the direction of waves as they pass through an opening or go around a barrier in their path.

Reflection, refraction, and diffraction are all associated with the bending of the path of a light wave on interaction with a physical boundary [1,2]. This bending of the path taken by light is an observable property, provided the medium is either two- or three-dimensional. Reflection occurs when light waves bounce off a barrier. The reflection of waves from smooth flat barriers follows the geometric laws of reflection. On the other hand, though the reflection of waves from parabolic or spherical barriers follows the laws of reflection to result in the convergence of the waves; the convergence need not necessarily be at the exact focal point. Similarly, when waves travel from one medium to another, a change in the direction of waves occur due to refraction. However, refraction is always accompanied by a change in wavelength and speed. Diffraction involves the bending of waves around obstacles and openings at oblique angles. In order to understand imaging performance, such as the resolution of various microscope objectives, it is necessary to study the diffraction property of light waves. Diffraction problems are amongst the most difficult problems encountered in optics. Due to their mathematical complexity, approximation methods are employed to solve diffraction problems. We describe the popular Huygens and Fresnel's approximation and extensions below.

3 Huygens-Fresnel Principle

The basis of optical wave propagation in geometrical optics is based on the propagation of wavefront. A wavefront is a surface over which an optical wave has a constant phase. The direction of propagation of the wave is always perpendicular to the surface of the wavefront at each point. Based on this concept of optical wave, Huygens postulated the formation of wavelets to describe the diffraction of light. Huygens's postulates [1,3] are

 I. Each element of a wavefront of light may be considered to be the centre of a secondary disturbance that gives rise to a spherical wavelet (Fig 1(a)).

 II. The position of the wavefront at any later time is given by the envelope of all such wavelets (Fig 1(a)).

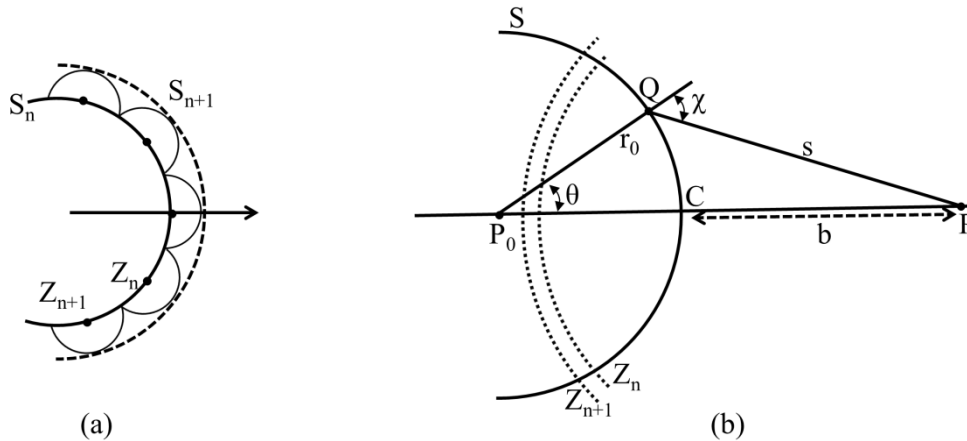III. The frequency and speed of the wavelets are the same as those of the primary waves.

(a)   (b)

Fig 1. (a) A pictorial representation of Huygens' construction in 2D. S_n and S_{n+1} are two concentric wavefronts, where S_{n+1} is the latter instance of S_n in propagation. The points Z_n, Z_{n+1} are the centres of the secondary wavelets. The envelope of these secondary wavelets creates the next wavefront. (b) Pictorial representation of Huygens-Fresnel construction. The representation is a cross-section of 3D space. P_0 is the point source. S is the spherical wavefront, centred at P_0. As shown in (a) these (Z_n and Z_{n+1}) are the plane waves on spherical wavefront S and act as the secondary disturbance points: i.e., are centers of the circles drawn in (a). P is the point where the effect of diffraction is observed.

Though the postulates are sufficient to describe the bending of light, while it undergoes diffraction, these principles are unable to quantify the intensity distribution due to the diffraction process. Fresnel added the principle of superposition to these principles, and thereafter these postulates together are well-known as the Huygens-Fresnel principles. The postulate added by Fresnel is that *the amplitude at any latter point is the linear superposition of the previous wavelets* [1-3].

In Fig 1(b), S is the instantaneous representation of a spherical monochromatic wavefront of radius r_0, which is originated from a point source P_0. The disturbance due to diffraction is measured at a point P on the wavefront. Unless we place an aperture, there is no diffraction. In fact, aperture limits the Fresnel zones and hence diffraction occurs. The disturbance at any point Q on the surface S, can be represented by $A.e^{ikr_0/r_0}$ (a spherical wave), which, in turn, is the amplitude of light at point Q. The contribution to the observation point P, due to the smallest element of the surface dS at Q, is $dU(P)$, which is represented as:

$$dU(P) = K(\chi) \frac{Ae^{ikr_0}}{r_0} \frac{e^{iks}}{s} dS \tag{1}$$

where, k is the wavenumber, χ is the diffraction angle, and $K(\chi)$ is the 'inclination factor', which is maximum when $\chi = 0$ and minimum when $\chi = \pi/2$. From Fresnel's postulate, amplitude at any point P, from a wavefront of surface S, is the superposition of all the secondary wavelets, which is mathematically represented as:

$$U(P) = \frac{Ae^{ikr_0}}{r_0} \iint_S \frac{e^{iks}}{s} K(\chi) dS \tag{2}$$

4 Fresnel- Kirchhoff Diffraction

Diffraction at any point P, arising from the superposition of secondary wavelets that proceed from the wavefront surface S, lies in between the point P and the light source: this is the Huygens-Fresnel idea. However, Kirchhoff [1] first pointed out that the resulting Huygens-Fresnel integral is only a special case of a set of integrals that are the solution of the homogeneous wave propagation equation, over a closed surface.
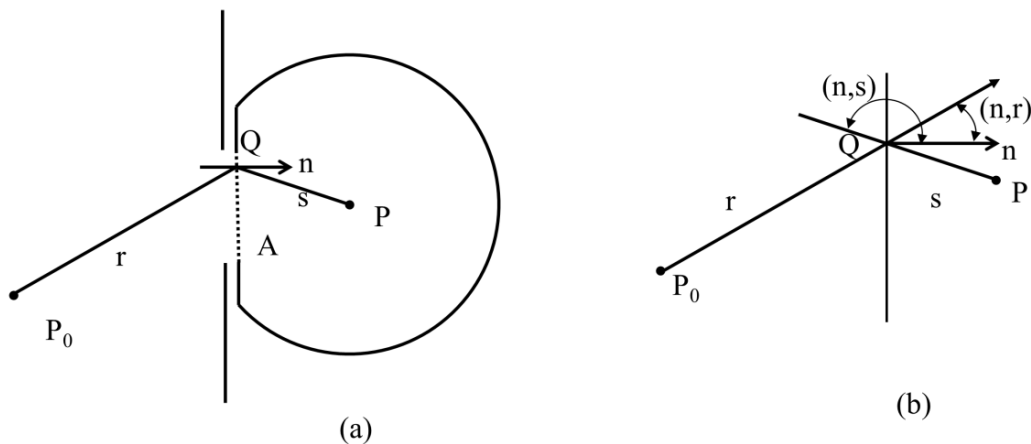

Fig 2. Pictorial representation of Fresnel-Kirchhoff's diffraction theory: (a) the diffraction at point P, originating due to the presence of the obstacle plane A in between the source P_0 and the observation point, P. The normal to the obstacle surface A is labeled as n. (b) A closeup of the intersection point is shown to illustrate that (n, r) and (n, s) are angles of incidence and diffraction, respectively.

The details of the mathematical formulation to solve the wave propagation equation (Helmholtz's equation) via Green's formulation are covered in details elsewhere [1]. The use of proper boundary conditions for diffraction at point P of Fig 1 (b) leads to the mathematical equation (A is the aperture):

$$U(P) = \frac{-iA}{2\lambda} \iint_A \frac{e^{ik(r+s)}}{rs} \left[\cos(n,r) - \cos(n,s) \right] dS \tag{3}$$

The Fresnel-Kirchhoff diffraction formula deals with only one diffracting surface, and in this regard, the formula is symmetric corresponding to the obstacle plane A (Fig 2a). This implies that the reversal of light source from P_0 to P does not change the diffraction equation. It is quite evident from the Fresnel-Kirchhoff's diffraction equation that the shape of the aperture and the position of the aperture to that of the source is the defining factor for the intensity distribution at point P. This Eq (3) collapses to the Huygens-Fresnel diffraction equation, where,(exp (ikr))/r represents a spherical wavefront.

The correct solution to a diffraction problem depends on the specification of the field on the boundary, i.e., on a diffraction plane A. In case of focusing using a high numerical-aperture objective, one usually follows the Debye theory (or the Debye approximation).

5 Diffraction of light in lens

Diffraction is employed to explain numerous phenomena, for example, the interaction of light with a grating structure and the behaviour of light under tight focusing. It is well-known that, even with a perfect lens, it is impossible to obtain an ideally focused point. In the focal region, the focusing spot displays an ellipsoidal shape instead of an ideal point. This ellipsoidal shape has a rotational symmetry along the optical axis. The dimension of the focal spot is characterized by the so-called longitudinal (L) and transverse (T) sizes of the spot. The ratio of these sizes (L/T) is often defined as the aspect ratio (AR).

The reason for the limited size (T, L) of the focusing spot is due to diffraction when light propagates through a lens aperture: lens aperture limits the size of the wavefront passing through it. Indeed, any diffraction aperture (i.e., a slit, a rectangular aperture or hole), a lens pupil, is constituted by an infinite number of diffracting points. Near the focal region, the EM field distribution is the superposition of all diffracted light rays that emerged from lens aperture (according to the Fresnel principle). The focusing spot is, therefore, an interference image of all these rays, and this results in a finite size that cannot be reduced below the diffraction-limit spot size, which depends on the wavelength of light.

The size and shape of the focusing spot have a direct impact on the resolving power of an optical microscope. For instance, the image of a point object on the camera is an image of the focusing spot, which is described by a point spread function (PSF). If there are two points located in the focal region, which are close enough to each other, the relevant PSFs overlap significantly and effectively merge into each other. This overlap of PSFs is the reason behind our incapability to distinguish the images of those points on the camera where the PSFs are overlapping. The exact definition of focusing spot size or minimum resolvable distance is an essential aspect of the optical microscope system, indeed for any imaging system. The mathematics and mathematical representation of resolution are described by two kinds of formulae proposed by Abbe and Rayleigh [1,2], respectively. The two formulae are quite similar and primarily differ only in their term coefficients, due to the different definitions of the minimum resolvable distance of two close point objects. In an imaging system, the Rayleigh criterion (two components of equal intensity should be considered as resolved when principal intensity maxima due to one-point source falls over the first intensity minima due to the other point source) is often considered to be the standard definition. In this case, the minimum resolvable distance between two close points is the distance at which the maximum intensity of relevant PSF of the first point just overlaps with the first minimum of the PSF of second point. This distance is equal to half of the size of a single PSF. In the Rayleigh criteria, the transverse and longitudinal minimum distances are given as follows [2]:

for the transverse (lateral) size:

$$T/2 = \frac{0.61\lambda}{\text{NA}} \tag{4a}$$

for the longitudinal (axial) size:

$$L/2 = \frac{2\lambda}{NA^2} \qquad (4b)$$

where λ is the wavelength of light, NA is the numerical aperture of the optical lens, which is defined as:

$$NA = n \sin \alpha$$

where n is the refractive index of the medium in which the light propagates, and α is half of the maximum angle that the imaging system accepts.

In order to achieve a tightly localized field or to achieve better resolving power, high NA optical lenses are often employed in microscope systems. The Rayleigh criterion is determined based on the intensity profile of the Airy disk, which is the diffraction pattern of a circular aperture. This diffraction is quantitatively studied by using the Fresnel-Kirchhoff scalar diffraction theory, in which the vector properties of light are omitted, and the direction of energy flow (Poynting vector) is also ignored. Hence, the intensity distribution on the focal spot only partially reflects the behaviour of the focusing spot size. However, when working with an optical system with a high NA optical lens, there are numerous fascinating phenomena, which can emerge, such as hollow focusing structures, asymmetric focusing behaviour, etc. When describing systems that show imaging via high NA objective lenses, a diffraction theory considering the vectorial properties of incident light is necessary.

6 Vectorial Imaging: Intensity and polarization distribution near focal plane of a high numerical aperture objective lens

In an optical imaging system, if the NA of the optical lens is relatively high (> 0.7), as shown in Fig 3, the wavefront (S_n) of the light beam at the exit of the objective is significantly curved and has a spherical form. Hence, the approximations taken in the scalar diffraction theory, including the paraxial approximation, Kirchhoff boundary conditions, Fresnel, or Fraunhofer approximations [3,4], are no longer satisfied. Correspondingly, the results derived from these approximations are not able to accurately reflect the behaviour of the light field distribution in the vicinity of a focal point. In 1950s, Richard and Wolf proposed a complete mathematical representation of EM field distribution in the focal region of a high NA optical lens [4]. Their proposed formula considers the vector properties of the EM field, and the derivation is based on the vectorial Debye approximation.
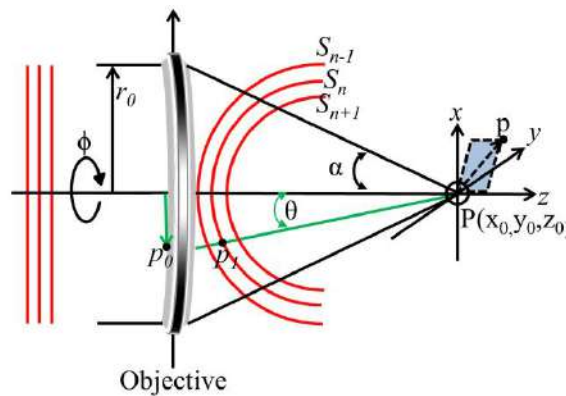

Fig 3. Geometrical representation of the propagation of light through a high NA lens (objective). Linear wavefronts transform to spherical wavefronts (S_n) after passing through the objective and focus onto point P. A diffraction picture at any point 'p', which is at a close proximity of the focal spot, is given by the Debye-Wolf integral.

The main principles of the Richard and Wolf theory may be summarized as follows [3, 5]:

1. The wavefront of the beam just after exiting the pupil has a spherical shape (Gaussian reference sphere) with a radius of f that is called the focal length of the optical lens.

2. Each secondary wavefront on the Gaussian reference sphere is considered to be a plane wave and is propagating towards the geometrical focal point of the lens.

3. Diffraction in the focal plane is the superposition of the entire plane wave on the spherical wave-front.

Following Richard and Wolf, the electric field distribution at an arbitrary point p (Fig 3) in the focal region is given in Cartesian coordinates [4-6] by:

$$\vec{E}(p) = -\frac{ikf}{2\pi} \iint_{s_x^2 + s_y^2 \leq 1} \vec{E}(s) \exp(ik\vec{s} \cdot \vec{p} + \frac{ds_x \, ds_y}{s_z}$$

$$= -\frac{ikf}{2\pi} \iint_{\Omega} \vec{E}(s) \exp[ik\{\Phi(s_x, s_y) + s_x x + s_y y + s_z z\}] d\Omega \tag{5}$$

where, f is the focal length, $k = 2\pi n/\lambda$ is the wavenumber, λ is the wavelength of the incident light, n is the refractive index of the immersion medium, and Ω is a solid angle of the objective aperture. Only inside this Ω angle, the diffracted light rays are considered to propagate towards the focal point and thus contribute to the formation of a tight focusing spot. A dimensionless vector, $s = (s_x, s_y, s_z)$, is considered to be pointing towards the geometrical focal point $P(x_0, y_0, z_0)$. $\Phi(s_x, s_y)$ is the wavefront distortion with respect to the Gaussian reference sphere in case of the presence of any aberration. Let 's' also refer to the amplitude distribution of light at the exit of the objective pupil (this is the transfer of the linear wavefront to the spherical wavefront on the Gaussian reference sphere). The exact expression of this term depends on different parameters, such as the apodization of the objective pupil, the input vector field, intensity, and phase distribution of the input light.

The physical interpretation of the Debye-Wolf integral is that the EM vectorial field distribution at an arbitrary point $p(x, y, z)$ in the focal region of a high NA optical lens is the superposition of all the diffracted plane waves that is represented by s, which emerge from the exit of lens within the solid angle Ω. Moreover, the field amplitude of the plane wave, s, have a direct relationship with the lens used and the incident vector beam.

For a conventional imaging system, i.e., an optical lens aperture of a circular shape, a spherical coordinate system can be introduced. The origin of the coordinate system is the geometrical focal point P. The wavefront (S_n) of the diffracted beam at the exit of the objective aperture is axially symmetric around the optical axis. In this spherical coordinate system, the Pointing vector s can be represented as [5,7], $\vec{s} = (\sin\theta \cos\phi \vec{i}, \sin\theta \sin\phi \vec{j}, \cos\theta \vec{k})$. Here, $(\vec{i}, \vec{j}, \vec{k})$ are the basis vectors in the x, y and z directions defined in Fig 3. α is the maximum focusing angle of the optical lens (directly related to the NA of the optical lens) with the relationship $0 < \theta \leq \alpha$ and ϕ is the azimuthal angle of the object plane. In this spherical coordinate representation, the solid angle can be expressed as $d\Omega = ds_x ds_y/s_z = \sin\theta \, d\theta d\phi$, where s_z is taken as direction cosine while in this equation it is distance. Therefore, the term $\exp\{ik(\vec{s} \cdot \vec{p})\}$ in the Debye-Wolf integral, Eq (5), transforms in the spherical coordinate system to:

$$\exp\{ik(\vec{s} \cdot \vec{p})\} = \exp\{ik\{x \sin\theta \cos\phi + y \sin\theta \sin\phi + z\cos\theta)\} \tag{6}$$

and the integral becomes:

$$\vec{E}(x, y, z) = -\frac{ikf}{2\pi} \int_0^\alpha \int_0^{2\pi} \vec{E}(\theta, \phi) \exp[ik(x \sin\theta \cos\phi + y \sin\theta \sin\phi + z \cos\theta) \sin\theta \, d\theta d\phi \tag{7}$$

$$\vec{E}(\theta,\phi) = A(\theta,\phi)\, B(\theta,\phi)\vec{P}(\theta,\phi) \tag{8}$$

The electric field distribution after exiting from the pupil of the optical lens is due to three separate terms, amplitude $A(\theta,\phi)$, apodization factor $B(\theta,\phi)$ and polarization state $\vec{P}(\theta,\phi)$ of the incident beam.

- $A(\theta,\phi)$ is the amplitude distribution of the incident beam and refers to the different beam modes (TEM_{00}, TEM_{10}, Bessel-Gaussian, etc.). For a uniform beam, $A(\theta,\phi) = 1$. When intensity and phase masks are used to alter the amplitude distribution of the incident beam, $A(\theta,\phi)$ changes accordingly.

- $B(\theta,\phi)$ is the apodization factor, which indicates the conservation of energy before and after the interaction of the electric field with the lens aperture. In an aplanatic lens system, Abbe's Sine Condition [1,5] for the ray projection is considered. For this, the apodization factor is $B(\theta,\phi) = \sqrt{\cos\theta}$.

- $\vec{P}(\theta,\phi)$ indicates the polarization state of an EM field in the focal region. It is expressed as $\vec{P}(\theta,\phi) = \vec{P_0}(\theta,\phi)T(\theta,\phi)$, where $\vec{P_0}(\theta,\phi)$ is a matrix of the polarization vector of the incident beam, and $T(\theta,\phi)$ is the appropriate transfer function. $T(\theta,\phi)$ is a 3×3 lens operator matrix that converts polarization of the object region to the focal region. The mathematical matrix representation is as follows:

$$P_0(\theta,\varphi) = \begin{bmatrix} p_x(\theta,\varphi) \\ p_y(\theta,\varphi) \\ p_z(\theta,\varphi) \end{bmatrix}. \text{ For x linear polarization, } P_0(\theta,\varphi) = \begin{bmatrix} 1 \\ 0 \\ 0 \end{bmatrix}$$

The transfer matrix [7] is again a combination of rotational transformations around the optical axes and is represented as:

$$T(\theta,\phi) = R^{-1}(\phi)\, L(\theta)\, R(\phi) \tag{9}$$

$R(\phi)$ is the rotation around propagation axis z, and $L(\theta)$ denotes the rotation around the perpendicular axis to that of the propagation axis. As the system coordinate representation is rotationally symmetric, it does not matter whether it is a left or right circular rotation. $R^{-1}(\phi)$ is the inverse rotation around the propagation axis. $T(\theta,\phi)$ only indicates the polarization conversion of the incident beam in case of homogeneous media. If there are any dielectric interfaces after the lens aperture, Fresnel coefficients must be introduced to consider the different transmissions of each polarization.

$$R(\phi) = \begin{bmatrix} \cos\phi & \sin\phi & 0 \\ -\sin\phi & \cos\phi & 0 \\ 0 & 0 & 1 \end{bmatrix}, \qquad L(\theta) = \begin{bmatrix} \cos\theta & 0 & \sin\theta \\ 0 & 1 & 0 \\ -\sin\theta & 0 & \cos\theta \end{bmatrix}$$

The total polarization vector in the focal region becomes

$$\vec{P}(\theta,\phi) = T(\theta,\phi)\vec{P_0}(\theta,\phi) = R^{-1}(\phi)L(\theta)R(\phi)\,\vec{P_0}\,(\theta,\phi) \tag{10}$$

The mathematical form of the transfer function and the components of the polarization field in the focal region is

$$\vec{P}(\theta,\phi) = \begin{bmatrix} 1+(\cos\theta-1)\cos^2\phi & (\cos\theta-1)\cos\phi\sin\phi & -\sin\theta\cos\phi \\ (\cos\theta-1)\cos\phi\sin\phi & 1+(\cos\theta-1)\sin^2\phi & -\sin\theta\sin\phi \\ \sin\theta\cos\phi & -\sin\theta\cos\phi & \cos\theta \end{bmatrix} \begin{bmatrix} \vec{P_x}(\theta,\phi) \\ \vec{P_y}(\theta,\phi) \\ \vec{P_z}(\theta,\phi) \end{bmatrix}$$

The final form of Debye-Wolf integral is

$$\vec{E}(x,y,z) = -\frac{ikf}{2\pi} \int_0^\alpha \int_0^{2\pi} \left(\begin{matrix} A(\theta,\phi)\, B(\theta,\varphi)\vec{P}(\theta,\phi) \\ \exp\left[ik(x\sin\theta\cos\phi + y\sin\theta\sin\phi + z\cos\theta)\right] \end{matrix} \right) \sin\theta\, d\theta d\phi \tag{11}$$

while the component-wise representation is

$$\begin{bmatrix} \vec{E}_x(x,y,z) \\ \vec{E}_y(x,y,z) \\ \vec{E}_z(x,y,z) \end{bmatrix} = -\frac{ikf}{2\pi} \int_0^\alpha \int_0^{2\pi} \left\{ A(\theta,\varphi)\ B(\theta,\varphi) \begin{bmatrix} \vec{P}_x(\theta,\varphi) \\ \vec{P}_y(\theta,\varphi) \\ \vec{P}_z(\theta,\varphi) \end{bmatrix} \exp\left[ik(x\,\sin\theta\,\cos\varphi + y\,\sin\theta\,\sin\varphi + z\,\cos\theta)\right] \right\} \sin\theta\ d\theta d\varphi \tag{12}$$

Component wise intensity distribution and total intensity distribution in the focal region is

$$I(x,y,z) = I_x + I_y + I_z = |\vec{E}_x(x,y,z)|^2 + |\vec{E}_y(x,y,z)|^2 + |\vec{E}_z(x,y,z)|^2 \tag{13}$$

where I_x, I_y and I_z are the intensity distribution of the of x, y, z polarized components of the total intensity $I(x,y,z)$ in the focal region [3,5,7].

7 Numerical simulation: Simulation script based on MATLAB®

In principle, there are an infinite number of secondary wavefronts on the Gaussian reference sphere, and all of them contribute to the intensity and field distribution in the focal region of an optical lens. In practice, $\theta(0 \le \theta \le \alpha)$ and $\phi(0 \le \theta \le 2\pi)$ are discretized into a number of divisions. For numerical computations, the angle θ is discretized from 0 to α by an equally spaced steps of $\Delta\theta$, and accordingly, the azimuthal angle ϕ is discretized from 0 to 2π by an equally spacing step-size of $\Delta\phi$. θ and ϕ are discretized in N_θ and N_ϕ number of linear steps:

$\theta_1 = 0$

$\theta_m = \theta_{m-1} + \Delta\theta$, $(1 \le m \le N_\theta$, integer)

$\Delta\theta = \alpha/N_\theta$; and

$\phi_1 = 0$

$\phi_m = \phi_{m-1} + \Delta\phi$, $(1 \le m \le N_\phi$, integer)

$\Delta\phi = \alpha/N_\phi$

Consequently, the integral formula can be simplified by considering a discrete number of plane waves and replacing the integral by summation as

$$E(x,y,x) = C \sum_{m=1}^{N_\theta} \sum_{n=1}^{N_\phi} \begin{bmatrix} A(\theta_m,\phi_n)\ B(\theta_m,\phi_n)P(\theta_m,\phi_n) \\ exp\left[ikn(z\,\cos\theta_m + x\,\sin\theta_m\,\cos\phi_n + y\,\sin\theta_m\,\sin\phi_n)\right] \end{bmatrix} \sin\theta_m\,\Delta\theta\,\Delta\phi\ m$$

$$\tag{14}$$

Here C is a constant, which depends on the wavelength of light and focal length of the optical lens. For a uniform circular input field with x-linear polarization, the intensity distribution in the focal region from the numerical calculation is presented in Fig 4. In this case, the input wavelength (λ) is 800 nm, NA of the optical lens is 1.4 oil immersion ($\alpha = 67.53^\circ$). A focal region of 1.5 μm ×1.5 μm (X-Y plane) is considered. The numerical simulation has been performed with $N_x = N_y = 500$ and $N_\theta = N_\phi = 100$ discrete points in respective dimensions. The numerical simulation program script is written in Matlab®2010, and with in the program script, there are subroutines for different polarization and intensity distributions of the input beam. The point spread function (PSF), which is the resolution parameter for focused illumination, is represented by Fig 5. From the figure, one can easily visualize and confirm that there is a significant portion (15% of the total intensity) of electric field vectors, which are Z-axis oriented (z-polarized component), though, at the onset of the simulation, there is no z-polarized light present in the input beam. Contribution from the y-polarized part at the focal plane is negligible ($\sim 10^{-3}$ order of magnitude) [5].
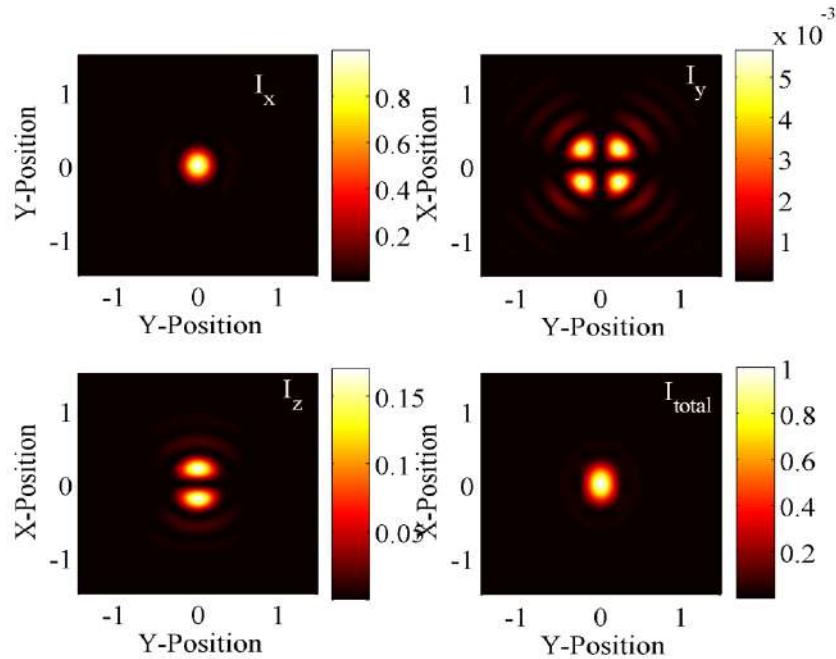
Fig 4. The relative intensity distribution in the focal plane (Transverse) for a uniform shaped beam $(A(\theta, \phi) = 1)$ is represented. The other parameters are NA = 1.4 for oil immersion objective lens, 800 nm wavelength, and x-linear polarization. Intensity is asymmetrically distributed in the X-Y plane. All axes are in μm.
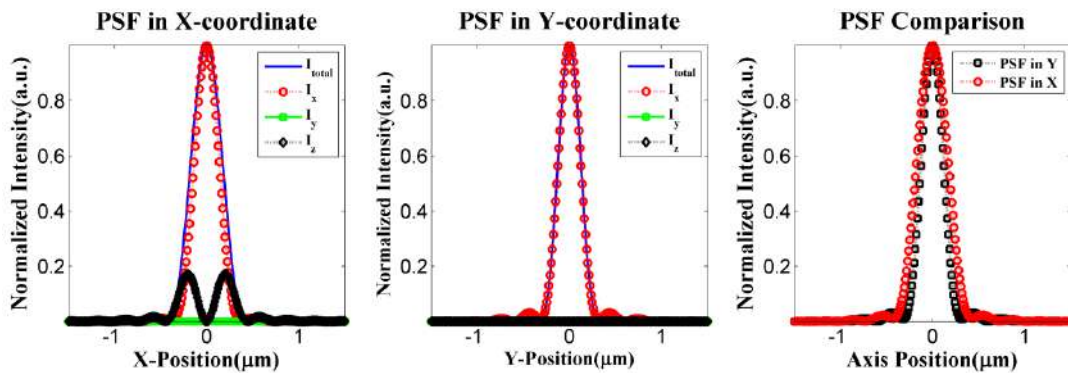

Fig 5. PSF of the different components of polarization is represented. There is a distinct separation in the resolution in the X-Y plane.

8 Experimental Evidence

In an optical tweezer measurement experiment, a particle is trapped in an optical field near the focal region of the optical microscope setup. A schematic setup of a typical single beam tweezer is shown in Fig 6, where both the focussing and collecting objective is the same.

Optical forces such as the gradient force field and the scattering force field require a delicate balancing in the focal region to ensure the spontaneous trapping of a microscopic particle. In this optically imprisoned condition, the trapped particle does not freeze totally. Though the random translational movement

is blocked, the particle still exhibits Brownian motion. Measuring the features of this Brownian motion, we are able to realistically probe and track the environment surrounding the trapped region and changes therein. To understand the Brownian motion of the trapped particle, one needs to know the exact trap stiffness, which is the measure of the strength of the potential well generated in the focal region. This potential well depends strictly on the intensity distribution of light in the focal volume [8].
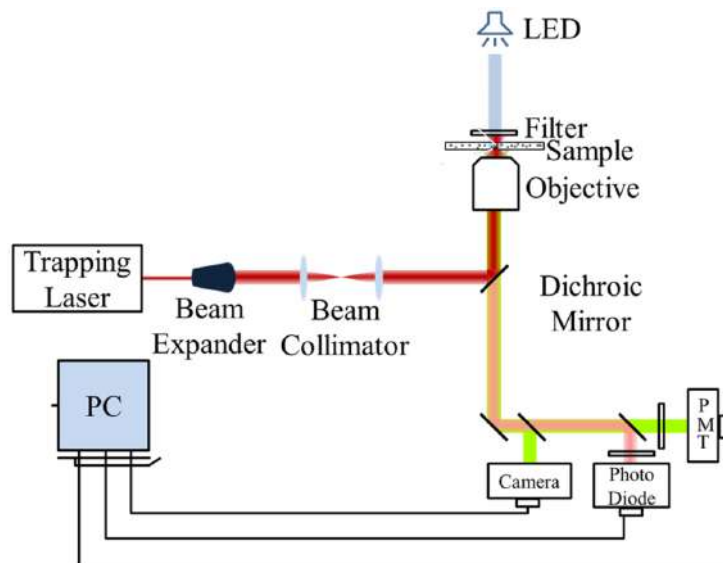

Fig 6. A schematic setup of a typical single beam tweezer showing the essential beam path through the microscope objective lens.

In practice, a Gaussian beam is used as a light source to generate a region where trapping will occur. It is assumed that the beam will generate a symmetric trapping region. Thus, it could be expected that the measurement of trap stiffness along either of the X-Y coordinates will yield the same result. In our experiment, we have trapped a 550 nm radius particle using an 800nm x-linearly-polarized pulsed laser beam and 1.4 NA oil immersion optical lens. The stiffness of the trapped region was measured in water and methanol. We measured the trap stiffness in the X- and Y- directions. The ratio of the stiffness measured in different directions is 0.754 in water and 0.7 in methanol. The intensity distribution ratio of a linearly polarized beam of light in the presence of 1.4 NA oil immersion optical lens is 0.78. This points to the fact there is an asymmetric intensity distribution in the focal region when working with a high NA optical lens.

9 Intensity distribution in the focal plane: Comparative Study

Diffraction plays a vital role in generating intensity distribution patterns in the focal region. This pattern is very helpful for the understanding of optical imaging, or for insights into the field of optical trapping. The 3D distribution pattern in the geometrical focal region depends on several parameters like polarization, intensity, phase, etc. of the input light. In the following sections, we have shown the differences in the intensity distribution, made by different parameters of the input light.

9.1. Intensity distribution in the focal region for different polarizations

The Debye-Wolf integral is different from the other scalar image theories, as the direction of the electric field (polarization) of the input beam plays an important role in the intensity distribution pattern. In 3D Cartesian coordinates, the polarization matrix (Jones Matrix) is defined in the Table 1 below.

Table 1. Polarization unit vectors and their patterns (Geometrical picture) are presented. ϕ is the azimuthal angle with respect to propagation axis z. In all cases, the input beam has rotational symmetry with respect to the z-axis.

Polarization	X-Linear	Y-Linear	Right circular	Left circular	Elliptical	Radial	Azimuthal
Pattern	$\updownarrow$	$\leftrightarrow$	◯	◯	⬭		
$\begin{bmatrix} p_x(\theta,\phi) \\ p_y(\theta,\phi) \\ p_z(\theta,\phi) \end{bmatrix}$	$\begin{bmatrix} 1 \\ 0 \\ 0 \end{bmatrix}$	$\begin{bmatrix} 0 \\ 1 \\ 0 \end{bmatrix}$	$\frac{1}{\sqrt{2}} \begin{bmatrix} 1 \\ i \\ 0 \end{bmatrix}$	$\frac{1}{\sqrt{2}} \begin{bmatrix} i \\ 1 \\ 0 \end{bmatrix}$	$\frac{1}{\sqrt{5}} \begin{bmatrix} 2 \\ i \\ 0 \end{bmatrix}$	$\begin{bmatrix} \cos\phi \\ \sin\phi \\ 0 \end{bmatrix}$	$\begin{bmatrix} -\sin\phi \\ \cos\phi \\ 0 \end{bmatrix}$
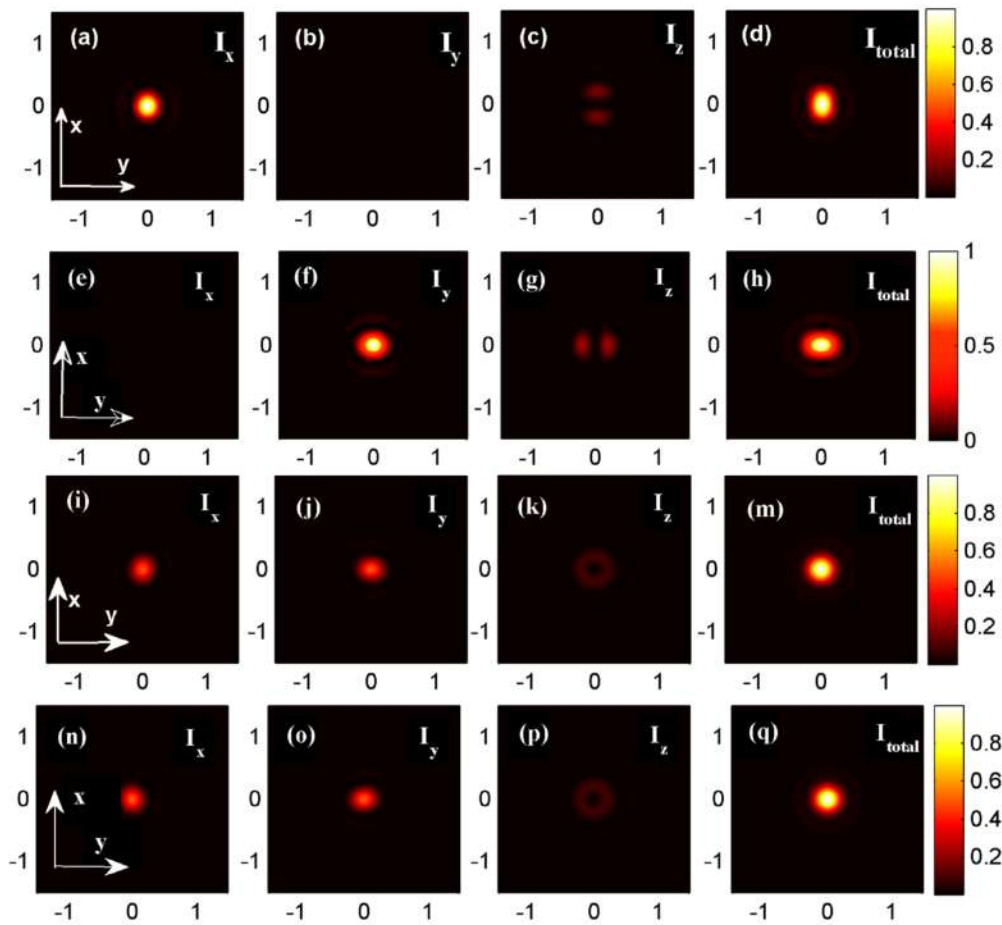
Fig 7. A uniform intensity input beam of 800 nm wavelength is focused using a 1.4 NA optical lens (oil immersion). Comparison between the intensity distribution at the focal plane (z = 0) for different input polarization is presented here for (a)-(d), X-Linear (e)-(h), Y-Linear (i)-(m), Right circular and (n)-(q) Left circular. All directional axes are shown in μm. For linear polarization cases, there are distinct asymmetric distributions of total intensity depending on the direction of polarization, but for the circular case, the total intensity distribution is symmetric in the X-Y plane.
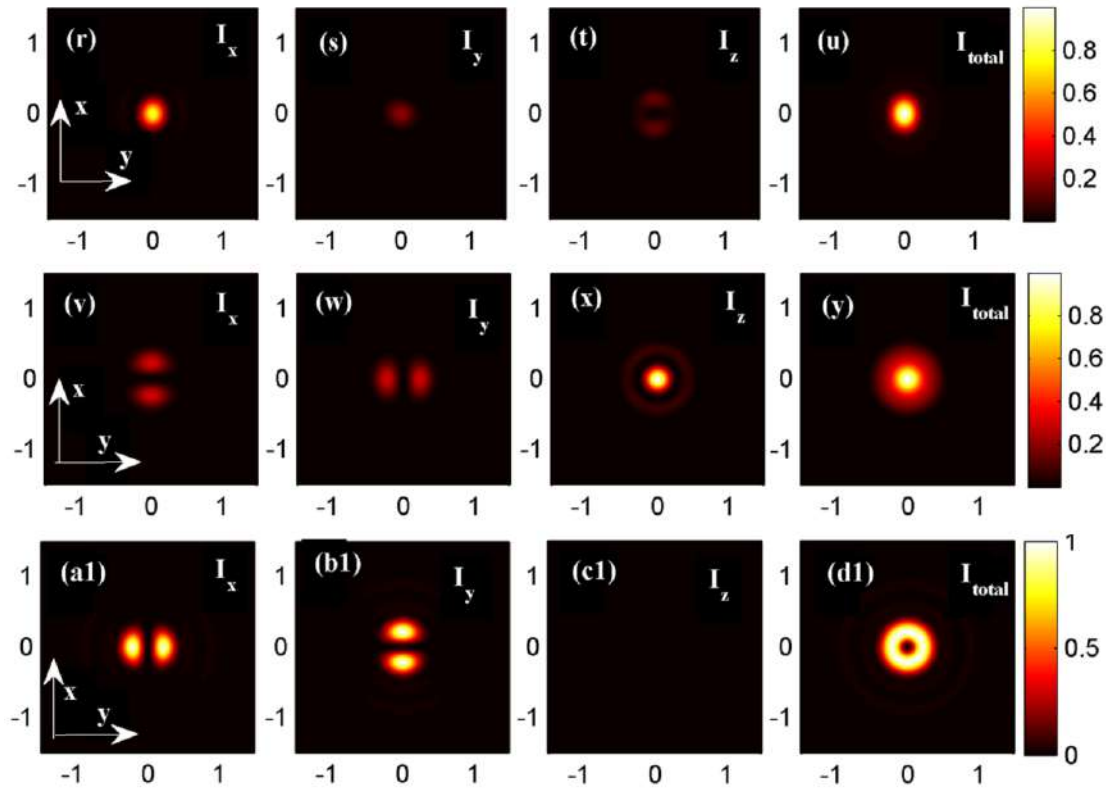
Fig 8. Comparison between the total intensity distributionin the focal plane for different input beam polarizations are presented here: Elliptical for (r)-(u), Radial for (v)-(y), and Azimuthal for (a1)-(d1). Other imaging parameters are for a uniform input beam. 1.4 NA optical lens(oil immersion) and 800 nm wavelength light. All directional axes are in μm.
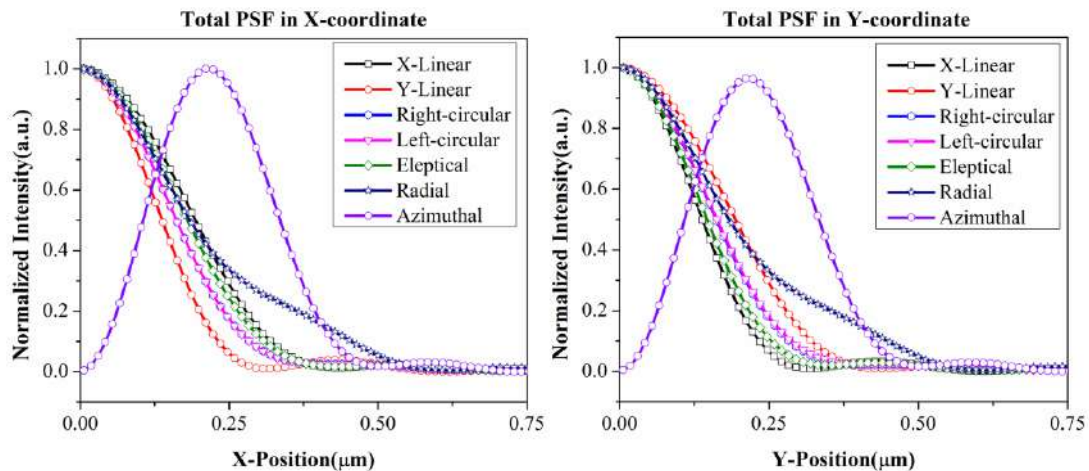

Fig 9. PSF for different polarizations along the two propagation axes. For the Azimuthal polarization, the shape is doughnut-like such that the peak position is 0.21μm away from the geometrical focal point.

Table 2. PSF values for different polarization cases showing resolution asymmetry predicted by vector imaging.

Polarization	X-Linear	Y-Linear	Right circular	Left circular	Elliptical	Radial	Azimuthal
x-coordinate	0.365 µm	0.285 µm	0.315 µm	0.315 µm	0.347 µm	0.348 µm	0.22 µm
y-coordinate	0.285 µm	0.365 µm	0.315 µm	0.315 µm	0.347 µm	0.348 µm	0.22 µm

Figures 7 and 8 show the total intensity distributions in the transverse plane at the focal point (z = 0) that are due to different input polarizations. Other imaging parameters are 1.4 NA optical lens (oil immersion), $A(\theta,\phi)$ =1, and an 800nm input wavelength. The full width at half maxima (FWHM) of the point spread function (PSF) for 1.4 NA optical lens at 800 nm wavelength would be 0.34 µm from the scalar field image equation (Eq 4(a)), which would also be without any asymmetric distribution in the transverse plane. Different polarizations of the input beam are also futile for scalar imaging as they are not accounted for. Vectorial imaging, using the Debye-Wolf integral, yields different point spread functions in the focal plane. For linear polarization inputs, there is a significant amount of asymmetry in the X-Y plane. On the other hand, for circular polarization inputs, there is no asymmetry, and for azimuthal polarizations, there is a doughnut-shaped point spread function. PSFs for different polarizations are presented in Fig 9. Table 2 lists the FWHM values of the PSFs.

9.2. Intensity distribution in the focal region for different NA optical lens

The NA of the optical lens is a crucial parameter for characterizing the optical imaging system as the NA is directly proportional to the limiting diffraction angle α. In our numerical simulation for NA dependence, we have taken four different NA optical lenses. Other input parameters are kept the same throughout the NA range. For a uniform input beam with X-linear polarization, increasing the NA increases the transverse as well as the longitudinal resolution (decreases the FWHM of PSF). The asymmetric ratio (PSF_y/PSF_x) for the transverse resolution increases as the NA of the optical lens decreases. For a 1.4 NA optical lens (oil immersion), the asymmetric ratio is 0.78, and for a 1 NA optical lens (oil immersion) the asymmetric ratio is 0.87. As the imaging system (optical lens) comes out of the high NA regime, the observed asymmetry in the PSF vanishes.

Figure 10 shows the intensity distribution of the focusing spot on the X-Z plane. A dramatic decrease of the focal spot size along the longitudinal direction with an increase of NA of the optical lens is observed, following a relation like that of the Rayleigh criteria (Eq (4b)).

Despite this dramatic decrease across different NA values (see Table 3), the longitudinal size (*L*) of the focal spot size is always larger than that along the transverse direction (T). This is because, when a single optical lens is used for focusing, it is only possible to collect or focus light in one direction, e.g., in the case being discussed, along the propagation direction or the Z-axis. All the light (and the associated information) in the other directions are missed. In order to further reduce the longitudinal focal size, one possibility is to use a 4-π configuration optical path [9], in which a second optical lens is placed on the opposite side of the first one to modulate the light field propagating along the optical axis of the system.

Table 3. Transverse (x-coordinate, y-coordinate) and longitudinal FWHM of PSF for different NA optical lenses.

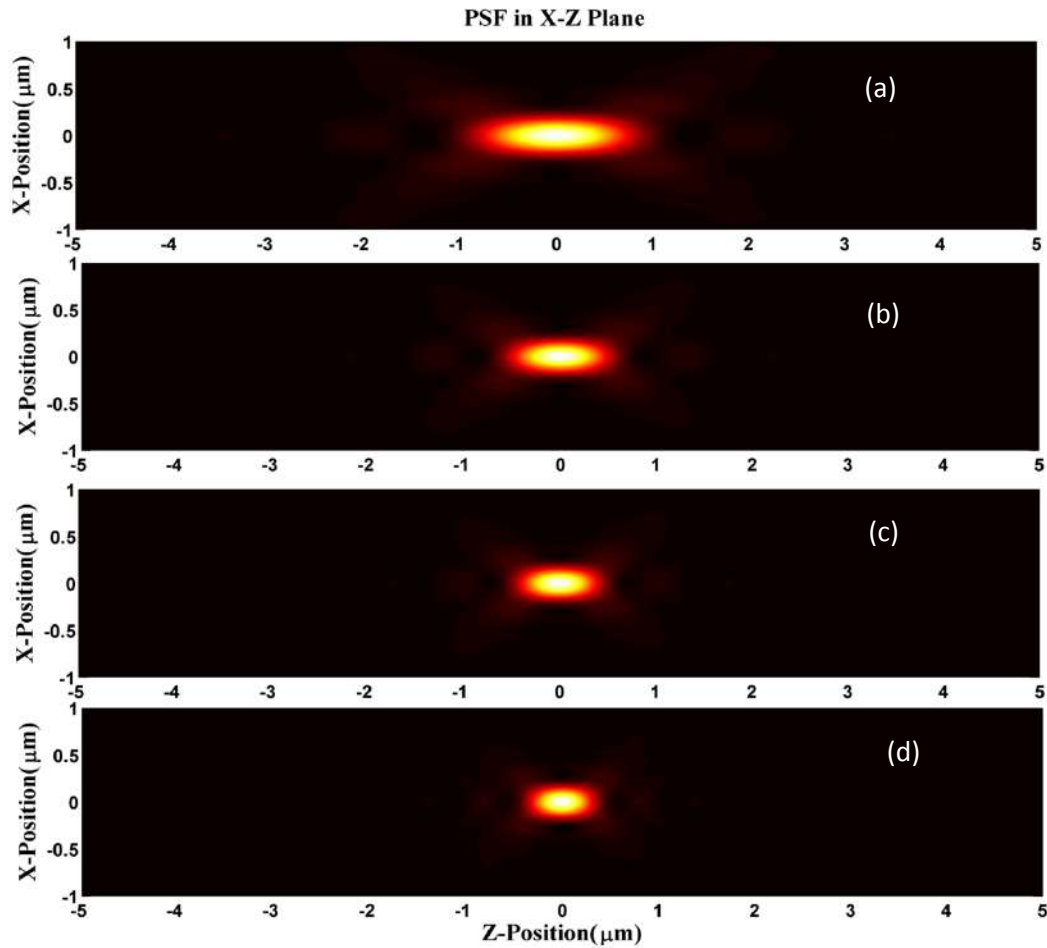| NA	x-coordinate	y-coordinate	z-coordinate
1.4	0.365 µm	0.285 µm	0.495 µm
1.3	0.377 µm	0.29 µm	0.615 µm
1.2	0.391 µm	0.317 µm	0.76 µm
1	0.44 µm	0.386 µm	1.175 µm

PSF in X-Z Plane

Fig 10. PSF in the propagation axis (z-axis) is shown for different NA optical lenses (oil immersion). (a) 1 NA optical lens (b) 1.2 NA optical lens (c) 1.3 NA optical lens (d) 1.4 NA optical lens. Other input parameters for the numerical calculations were: uniform intensity distribution, 800 nm wavelength and x-linear polarization of light. It is evident that depth of focus decreases as NA increases.

9.3. Intensity distribution in the focal region for different input beam profile

The laser beam is often employed as a light source; it is thus important to characterize the focusing behaviour of different laser beams under tight focusing conditions. The most frequently used beams are the Gaussian beams (TEM$_{00}$), and the Bessel-Gaussian (B-G) beams. In the case of the Gaussian beam, the beam waist is the determining factor for the generation of focal spot resolution [10-14].

For a 1.4 NA optical lens (oil immersion), two cases of Gaussian beam with different FWHM are considered for numerical calculation and comparison. Each beam is x-linear polarized. The mathematical input form of the Gaussian beam is represented in Table 4, where a is the parameter that represents the beam waist at the entrance pupil. Here two cases, a =1 and a =3 are considered, where the argument is $\beta = (\sin\theta/\sin\alpha)$. Profiles shown in the first column of Fig 11 represent Gaussian input beams. The second column in Fig 11 shows the total intensity distribution in the X-Z plane of the focal region for the respective Gaussian input beams inputs of the first column.
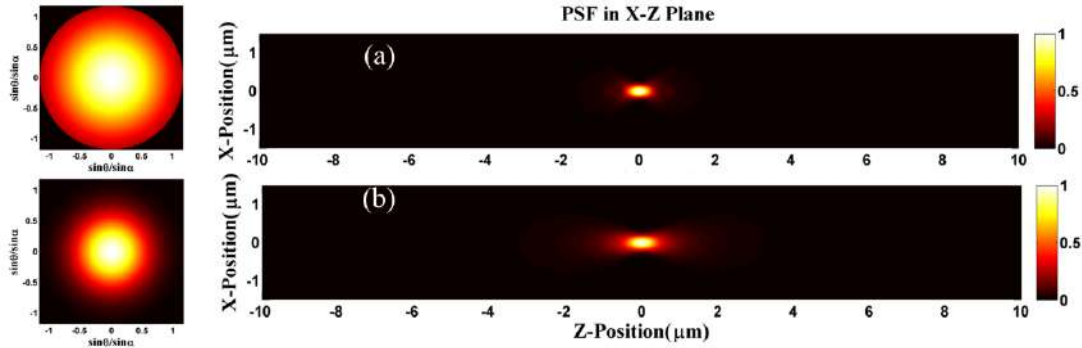
Fig 11. Two Gaussian beam inputs and their corresponding total intensity distributions at the X-Z plane near the focal region. (a) is for $a = 1$ and (b) is for $a = 3$. Numerical calculation parameters are 1.4 NA optical lens, x-linear polarization, 800 nm input beam.

Compared to the uniform beam case (Fig 12), Gaussian beams allow obtaining very similar intensity distributions but with larger spatial resolution in both the cases (longitudinal and transverse). In the case when $a = 1$, the Gaussian is of the form: $\exp(-\beta^2)$, and the resolution in both planes is almost similar to that of the uniform input beam. When $a = 3$, the Gaussian is of the form: $\exp(-3\beta^2)$, and the resolution decreases as the beam waist becomes narrower. This can be explained by the fact that the light intensity of the Gaussian beam is concentrated in the beam centre, which is equivalent to the sum of a large aperture of one of the uniform beams (high NA) and a small aperture of a uniform beam (low NA). Hence, the resultant intensity distribution is larger than the one obtained with a single uniform beam (high NA).
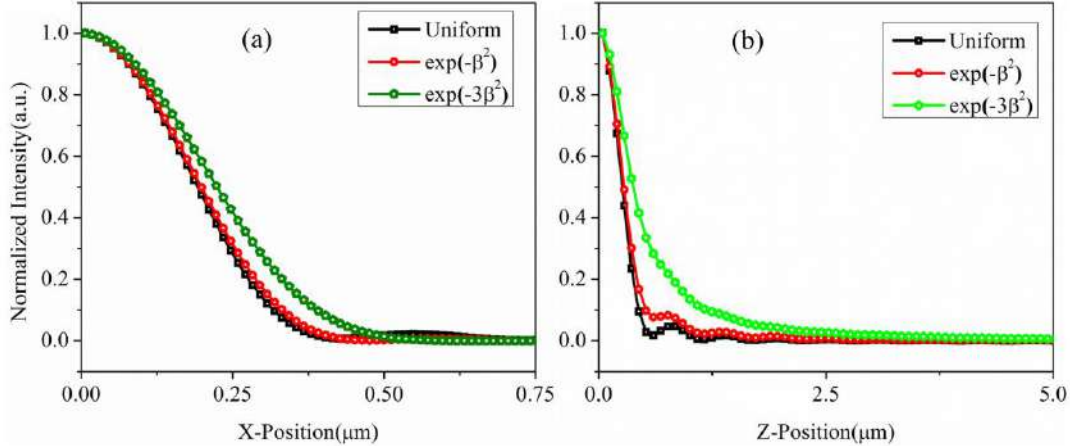

Fig 12. Comparison of different input beams. (a) resolution comparison in X-direction. (b) resolution comparison in Z-direction (longitudinal).

When the Bessel-Gaussian (B-G) beam (x-polarized) is taken as an input, the shape of the intensity distribution in the focal region for both planes changes drastically from case to case. Table 4 shows the amplitude profile for a few beam modes including the generic B-G beam. As the parameter a increases (the number of rings in the input aperture increases with increase in the value of a), we can see that the intensity at the focal spot ($x = 0, y = 0, z = 0$) vanishes (Fig 13(d)). The intensity distribution forms an annular ring-like structure in the focal plane. Figures in first column of Fig 13 represent different Bessel-Gaussian input beams.

The first two cases, where input beam looks like Gaussian, yield intensity distribution at the focal plane, which is almost similar to that of corresponding to a Gaussian input. However, as the ring in the input beam increases (in the case of $a=5$, $a=10$), it leads to the formation of a ring-like structure in the focal plane (Fig 14). The ring structure for B-G input, $J_0(5\beta)\exp(-\beta^2)$, the width of the ring is 0.88 μm, and the FWHM width of the intensity profile is 0.34 μm. For the B-G input, $J_0(10\beta)\exp(-\beta^2)$, these values are 1.8 μm and 0.336 μm. We observe that as the number of rings in the input increases, the diameter of the annular ring-like intensity distribution in the focal region increases, and the spatial resolution of this ring-like structure remains almost unchanged (Fig 15 (a)).

Table 4. Different beam modes used to calculate the intensity distribution in the focusing region of a high NA optical lens. $A(\theta,\phi)$ represents the amplitude of the beam mode. α is a generic parameter describing different beam waists. β is the ratio of $\sin\theta/\sin\alpha$. θ and ϕ are the polar coordinates of the lens aperture (see Fig 3). J_0 is the generalized Bessel function of order zero.

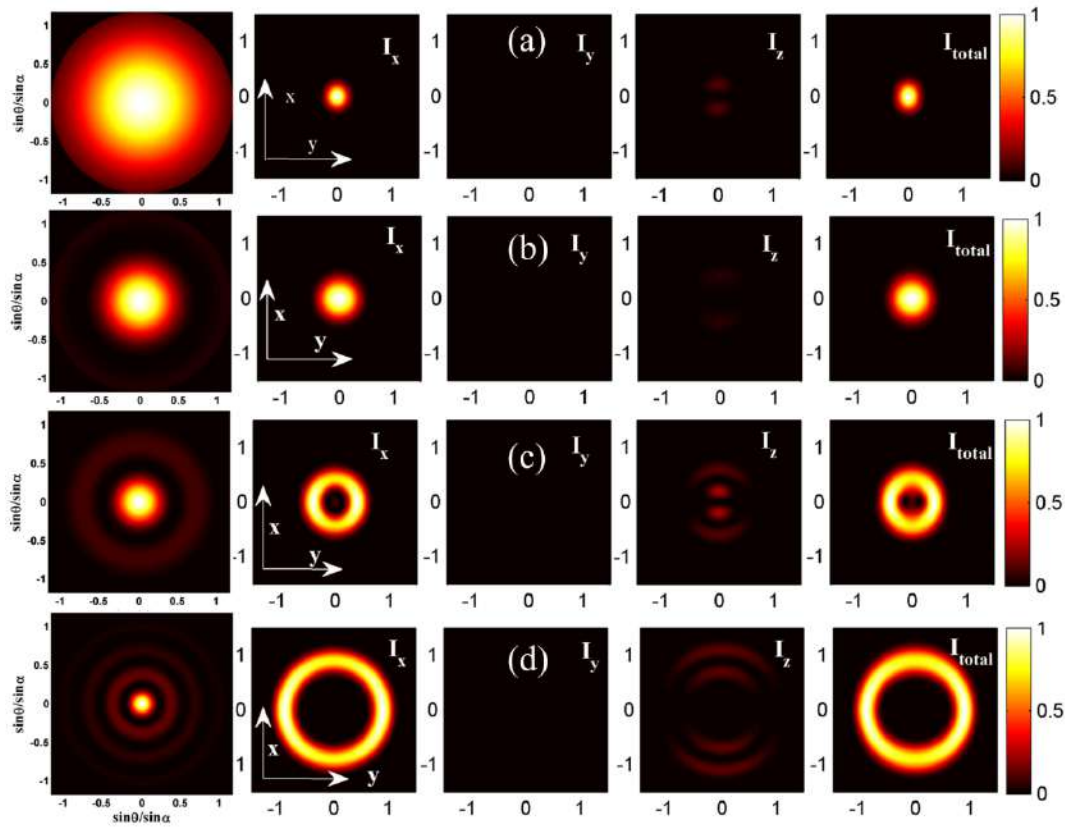|	
Uniform beam	$A(\theta, \phi) = 1$
Gaussian beam	$A(\theta, \phi) = \exp(-a\beta^2)$
Bessel-Gaussian beam	$A(\theta, \phi) = J_0\exp(a\beta) \exp(-\beta^2)$

Fig 13. Intensity distribution of Bessel-Gaussian beams at the focal plane (X-Y plane) with different a values. (a) is for $a =1$, (b) is for $a =3$, (c) is for $a =5$, (d) is for $a =10$. Numerical calculation parameters are 1.4 NA optical lens, x-linear polarization, 800 nm input beam.

We investigate the anomalous features of certain kinds of B-G beam (where parameter a is 5, 10, or higher) in terms of the intensity distribution in the X-Z plane (longitudinal). In Fig 11, the numerical simulation of the intensity distribution in the X-Z plane is shown. It is clear from the figure that in the propagation path, both beams first focus before the actual focal spot ($x = 0$, $z = 0$). As discussed before, in the focal spot, these beams form a hollow pattern and refocus again after the focal spot. This intensity distribution behaviour can be explained by the fact that the focusing spot is the consequence of the interference of diffracted light rays in the focal region. For B-G beams, the light of the inner and outer rings possess different phases, and thus, when the diffracted beams are added up in the focal region, they interfere destructively, and the total intensity at the focal point is weakened.
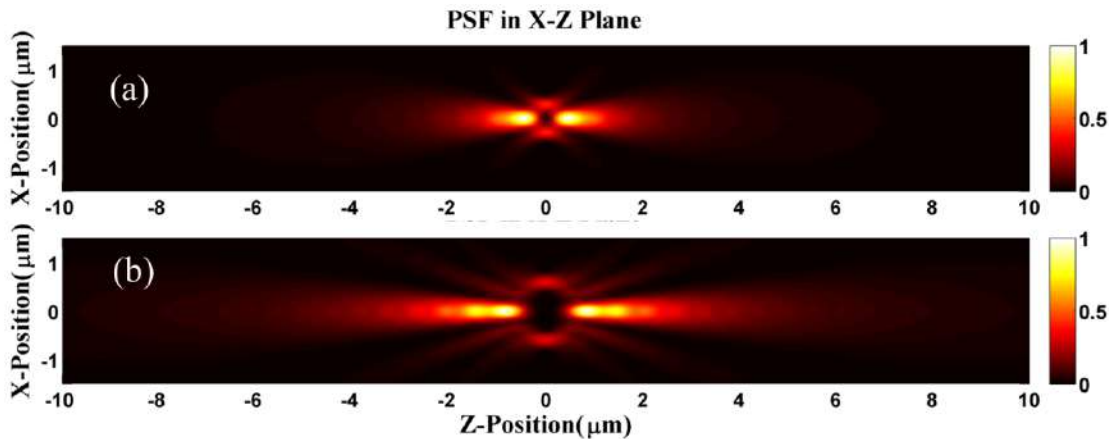

Fig 14. Total intensity distribution at the X-Z plane near the focal region of two Bessel-Gaussian beams, $J_0(a\beta)$ $\exp(-\beta^2)$ is represented here. (a) is for $a = 5$ and (b) is for $a = 10$. Numerical calculation parameters are 1.4 NA optical lens, x-linear polarization, 800 nm input beam.
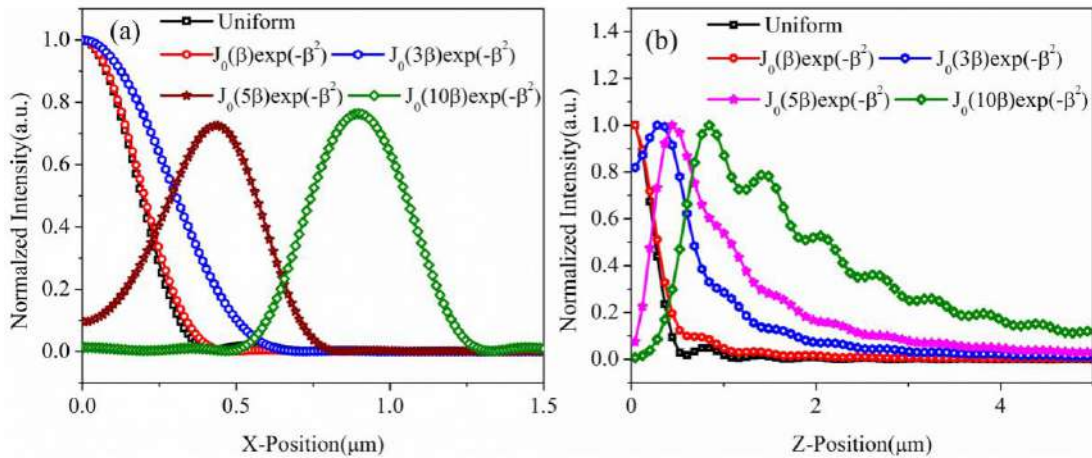

Fig 15. Comparison of different Bessel-Gaussian input beams. (a) resolution comparison in X-direction. (b) resolution comparison in Z-direction (longitudinal).

In Fig 15 (b), a comparison of the intensity distribution in the longitudinal plane among different B-G beams is represented. For the B-G beam with parameter $a = 5$, the separation between two intense spots, is 0.88 μm, whereas the separation is 1.68 μm, for the second case with parameter $a = 10$. Careful inspection

reveals that there are several intense regions in the longitudinal direction. The real challenge lies in making singular separate spots in the propagation.

This study shows that the intensity distribution of the focusing spots strongly depends on the profile of the incident beam. This is shown, for instance, when the beam profile is varied by using different laser beam modes. Over the next sections, we introduce alternative ways to modulate the incident beam profile and study their effects on the intensity distribution of tight focusing spots.

10 Intensity distribution in the focal region due to spatial masks

Masks are applied to modulate both the intensity and phase of the incoming beam profile. By using a proper mask, it is possible to transform the uniform plane wave to a particular desired beam shape, such as a hollow beam, phase singularity vortex beam, etc. There are three kinds of frequently used masks to modulate the spatial properties of the input light beam. These are amplitude masks, $0/\pi$ binary-phase zone plate (BPZP), and vortex masks [15-21]. These masks are designed to modulate light, which shows rotational symmetry around the optical axis. Hence, it is convenient to define the diffracted wave vector using spherical coordinates. When using a mask (to modulate the uniform beam), the $A(\theta, \phi)$ is tweaked accordingly to ensure the formation of the expected structure with the masks.

10.1 Amplitude Mask

The pictorial representation of an amplitude mask is given in Fig 16. Generic amplitude masks with rotational symmetry can be represented as

$$A(\theta, \phi) = \begin{cases} 1 & : (0 < \varepsilon \le \varepsilon_A) \\ 0 & : (\varepsilon_A < \varepsilon \le 1) \end{cases} \tag{15}$$

where, $\theta = \theta_A$ is the angle between the optical axis and the marginal edge line of the opaque inner area. As shown in Fig 16, $\varepsilon_A = \sin\theta_A / \sin\alpha$, where ε_A is the ratio of r_A and R ($\varepsilon_A = r_A/R$). A generic amplitude mask is designed to have an opaque area followed by a transparent area or vice versa (Fig 17 (a)). For the numerical calculations, we have taken an input beam of uniform amplitude and circular polarization. Other optical parameters are 1.4 NA optical lens (oil immersion) objective and 800 nm wavelength light. The intensity masks are labelled as C_1, C_3, and C_5 depending on the number of bright and dark ring pattern within the aperture of the objective.
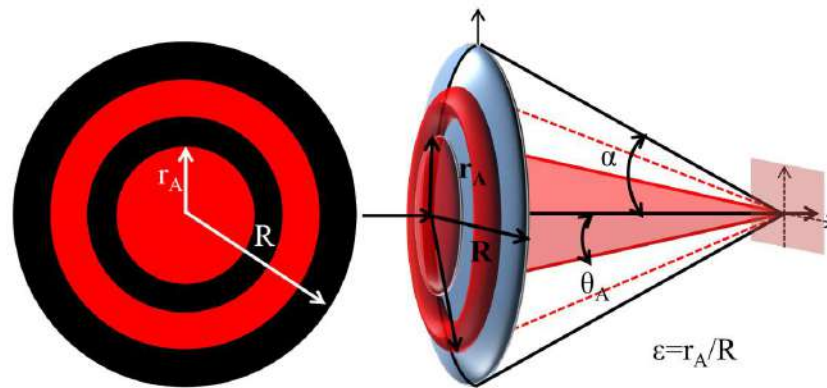

Fig 16. The geometrical representation of an amplitude mask that has a rotationally symmetric structure around the beam propagation axis. R is the outer radius of the beam and r_A is the inner radius of the beam. The ratio between these two is $\varepsilon_A = r_A/R = \sin\theta_A / \sin\alpha$

The intensity distribution in the transverse plane (X-Y) for all the cases (C_1-C_5) remains almost similar. The FWHM of the beams for C_1 is 0.3μm and, for C_3 and C_5 are 0.33μm. For a uniform beam with circular polarization and having no intensity-modulation the FWMH is 0.34μm (Fig 18 (b)). Intensity modulation alters transverse resolution very minutely or not at all. The intensity distribution in the propagation direction (X-Z plane) exhibits a significant change in spatial resolution due to amplitude masking. The FWHM of the intensity distribution due to an unmodulated uniform beam with circular polarization is 0.8 μm. The FWHM for the C_1, and C_3 cases are 0.44 μm, while that for C_5 case is 0.66 μm (Fig 18 (a)). Careful design of the intensity modulation leads to a better resolution in the Z-direction. Figure 19 shows the intensity distribution in the longitudinal plane.
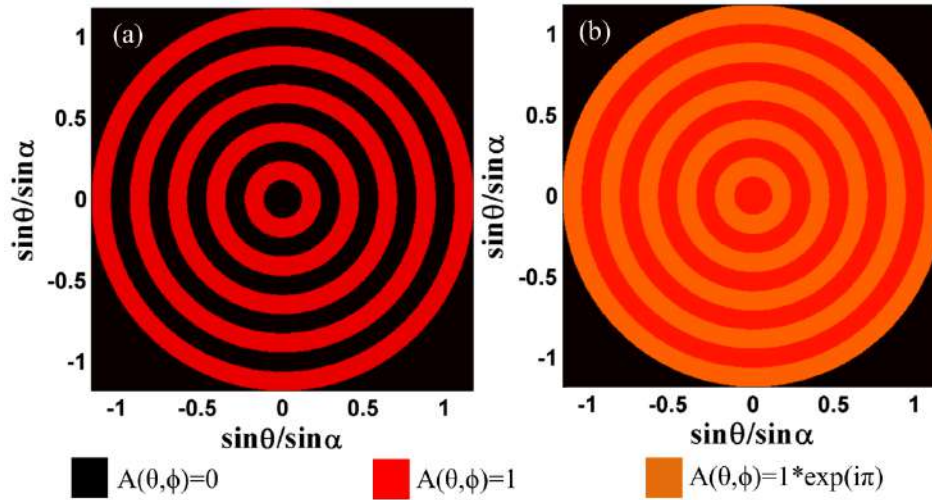

Fig 17. Intensity and binary-phase zone plate (BPZP) pictorial representation. (a) A spatial intensity modulator plate (C_5- five continuous regions of opaque and transparent zones), having a rotational symmetry around the optical axis. (b) A BPZP pictorial representation with five separate $0/\pi$ plates (C_5-BPZP).
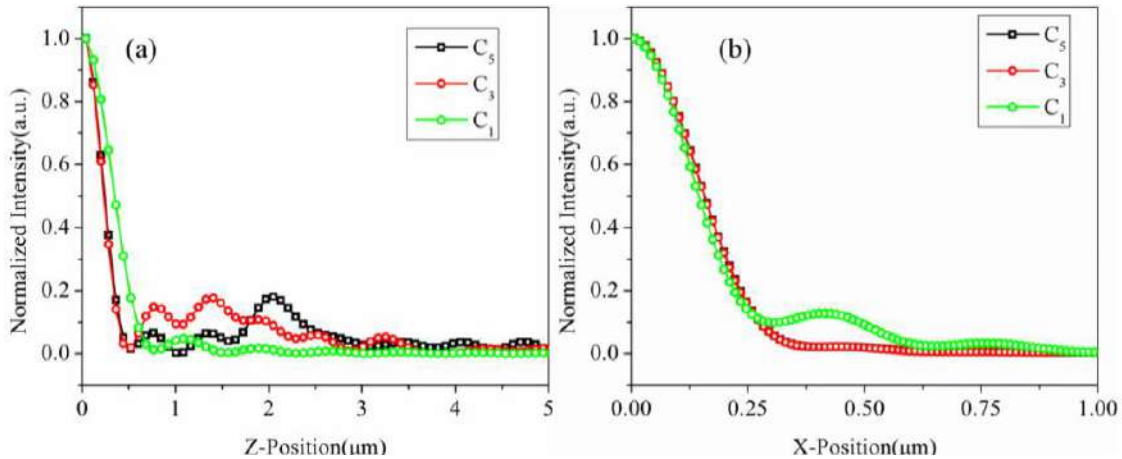

Fig 18. PSF in the focal region due to intensity modulation. (a) PSF in the Z-direction. (b) PSF in the X-direction. The other parameters are 1.5 NA optical lens (oil immersion), a uniform light beam with circular polarization, and 800 nm wavelength. Due to circular polarization, the PSF in the X-Y plane has no asymmetry.
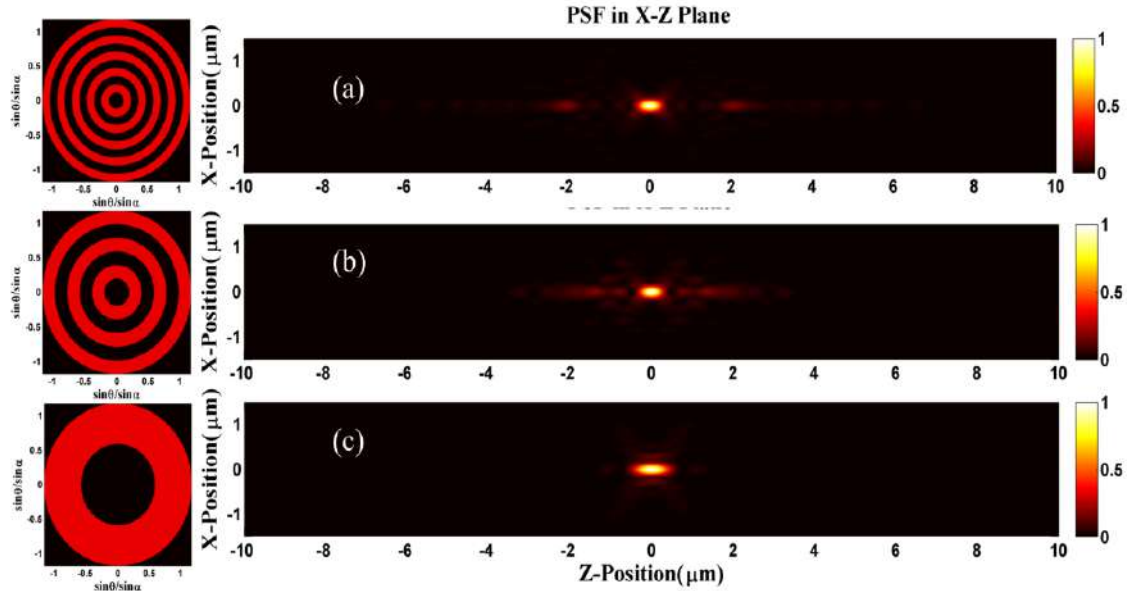
Fig 19. Intensity distribution in the longitudinal plane (X-Z) due to the application of intensity mask in front of the input. (a)-(c) are intensity distribution of C_5, C_3, and C_1, respectively. It is clear that the increase in the number of rings in the intensity modulation only tunes the focal spot structure and not the spatial resolution after certain threshold.

10.2. 0/π *Phase plate or binary-phase zone plate* (*BPZP*)

In this case, the adjacent concentric circular structures are not opaque and transparent like intensity masks, but the structures are phase-shifted by π to each other. The circular structures are of even and odd ring numbers and the phase of the BPZP [22] is set to π for the odd (or even) belt, while the even (or odd) one is set to 0. A generic representation of BPZP is shown in Fig 17 (b). The mathematical form of a BPZP is

$$A(\theta, \phi) = \begin{cases} \exp(i\pi) & : \pi - \text{Phase shift } (0 < \varepsilon \le \varepsilon_A) \\ \exp(i0) & : 0 - \text{Phase shift } (\varepsilon_A < \varepsilon \le 1) \end{cases} \tag{16}$$

For numerical calculations, we have taken three different cases: C_1-BPZP, C_3-BPZP and, C_5-BPZP, having one, three and, five pairs of concentric phase zone plates. The other input parameters are the circularly polarized beam of 800 nm wavelength and 1.4 NA optical lens objective.

Figure 20 shows the total intensity distribution pattern in the longitudinal plane (X-Z). The use of BPZP, in fact, splits the focal region into two separate spots. This behaviour can be also explained by the fact that due to the π−phase shift of the inner part of the incident beam, when the rays are adding up at the focal region, the phase difference of rays induces destructive interference at the focal point, while in its vicinity, rays are in phase and thus a constructive field distribution appears. An increase in the number of concentric BPZP in the path of input beam increases the separation between the peak in the propagation direction. For our case of C_1-BPZP, C_3-BPZP, and C_5-BPZP, the separations are 0.72μm, 2.48μm and, 4.1μm, respectively (Fig 21). The careful design of a BPZP with an appropriate NA optical lens will result in the generation of the desired spot separation along the propagation axis.
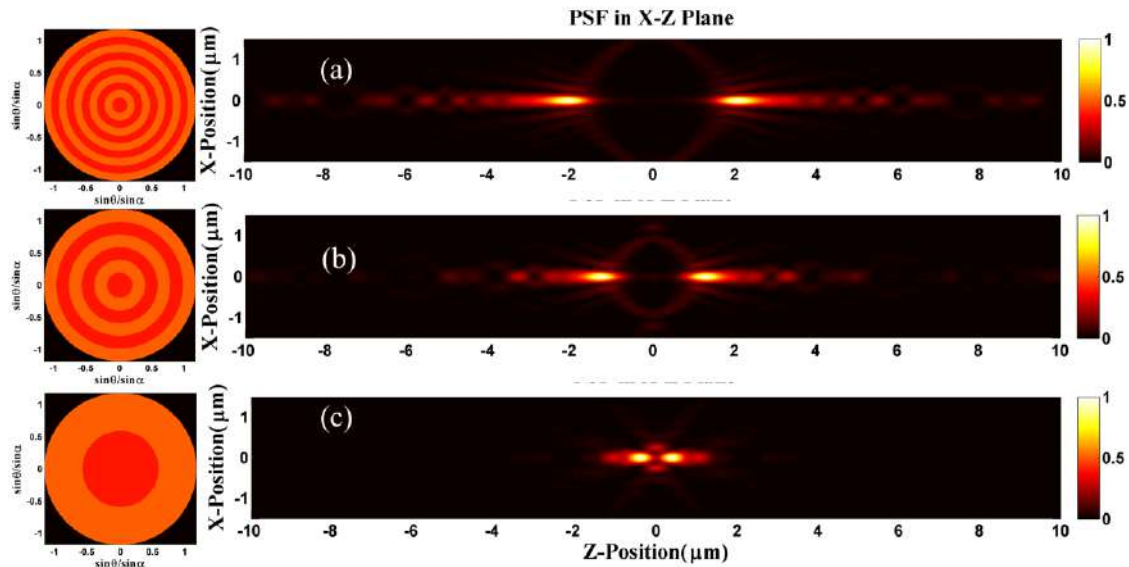
Fig 20. Total intensity distribution in the longitudinal plane due to the application of BPZP having a circular symmetry with respect to the propagation axis. (a)-(c) is a pictorial representation of the intensity distribution due to C_5-BPZP, C_3-BPZP, and C_1-BPZP, respectively. We note that the use of BPZP causes the formation of two separate intense spots in the propagation axis.

11 Aberration due to a stratified medium

In practice, one critical problem concerning the application of optical microscopy is an aberration, which degrades the resolution of the optical microscope or any optical setup with a high NA optical lens [23]. In an experimental setup, a minimum of at least three layers exist, as is shown in Fig (22). The first layer is the immersion medium, which in our case is oil. The second layer is the coverslip, and the third layer is the medium where the imaging object is placed (which, in most of the cases, is water). The oil-immersion medium and coverslip have almost the same refractive index. For practical purposes, one can consider these
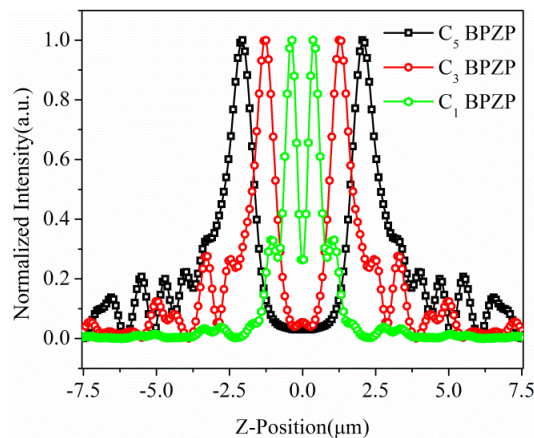

Fig 21. PSF due to the use of different BPZP to modulate input beam. It clearly shows that with the increase in the number of concentric BPZP belt, the separation of the peak increases.

two separate layers to be a single layer. Depending on the refractive index mismatch, there is a significant shift in the geometrical focusing point. In our case, when the medium in the sample chamber is water, the actual focusing happens before the geometrical focal point, as water has lower refractive index compared to glass [24-26]. This is the scalar imaging property of a lens. By quantitatively measuring this shift, one can determine the refractive index of the mismatch medium. However, for high NA optical lens systems, light rays converge significantly, and the transmission coefficients (Fresnel coefficient) of *s*- and *p*-polarization need to be considered [1].
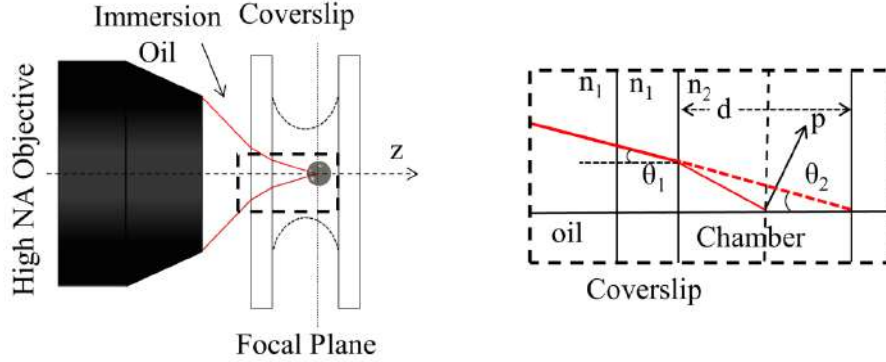

Fig 22. Schematic illustration of the propagation of a tightly focused beam in the presence of refractive index mismatch in the propagation path. In our system, the immersion medium and coverslip have the same refractive index. We consider them together as the first refractive index medium, n_1. The water medium is considered as second refractive index medium, n_2. If the medium were homogeneous ($n_1 = n_2$ case), the geometrical focal point would be distant d apart from the starting point of the second medium.

The transfer function to the Gaussian reference sphere changes due to the non-equivalent transmission of 's' and 'p' polarizations as well as due to the phase aberrations in the propagation path. Thus, the polarization transfer function (Eq 9) can be rewritten as:

$$P_1(\theta_1, \phi) = T_1(\theta_1, \phi)P_0 = R^{-1}(\phi)C(\theta_1)R(\phi)P_0 \qquad (17)$$

where P_1 is the polarization distribution in the medium of refractive index n_1, and θ_1 is the incident angle on the first medium. P_0 is the incident beam polarization. $R(\phi)$, and $C(\theta_1)$ describe the rotation of the coordinate system about the optical axis. The polarization distribution in the medium of refractive index n_2 is

$$P_2(\theta_1, \theta_2, \phi) = T_2(\theta_1, \theta_2, \phi)P_1(\theta_1, \phi) = T_2(\theta_1, \theta_2, \phi)T_1(\theta_1, \phi)P_0$$

where:

$$T_2(\theta_1, \theta_2, \phi) = [L^{(2)}]^{-1}IL^{(1)} \qquad (19)$$

and:

$$I = \begin{bmatrix} t_p & 0 & 0 \\ 0 & t_s & t_s \\ 0 & 0 & t_p \end{bmatrix}, \qquad L^{(i)} = \begin{bmatrix} \cos\theta_i & 0 & -\sin\theta_i \\ 0 & 1 & 0 \\ \sin\theta_i & 0 & \cos\theta_i \end{bmatrix}$$

which describes the rotation of the coordinate system into *s*- and *p*-polarized vectors, $i = 1, 2$ represent the light rays before and after the interface, I represents the transmission of the dielectric interface and t_s and t_p are the Fresnel coefficients:

$$t_s = \frac{2\sin\theta_2 \cos\theta_1}{\sin(\theta_1 + \theta_2)}, \qquad t_p = \frac{2\sin\theta_2 \cos\theta_1}{\sin(\theta_1 + \theta_2) \cos(\theta_1 - \theta_2)} \qquad (20)$$

Previously in Eq (11), we have omitted the aberration factor in the Debye-Wolf integral. Here, however, due to the presence of the interface of different refractive indices, one cannot neglect the induced aberration factor in the imaging system. This aberration is defined as:

$$\Phi(\theta_1, \theta_2, d) = -d(n_1 \cos\theta_1 - n_2 \cos\theta_2) \tag{21}$$

Using $\Phi(\theta_1, \theta_2, d)$ and $P(\theta_1, \theta_2, \phi)$, the Debye-Wolf integral can be rewritten as

$$\vec{E}(x, y, z) = -\frac{ikf}{2\pi} \int_0^\alpha \int_0^{2\pi} \left| \begin{array}{l} A(\theta_1,\phi)\, B(\theta_1,\varphi)\vec{P}_2(\theta_1,\ \theta_2,\ \phi) \\ exp\,[ik(n_1\,x\,\sin\theta_1\,\cos\phi + n_1\,y\,\sin\theta_1\,\sin\phi + n_2\,z\,\cos\theta_2)] \\ exp\,[ik\,(\Phi(\theta_1,\ \theta_2,\ \phi)] \end{array} \right| \sin\theta_1\ d\theta_1 d\phi \tag{22}$$

Using Eq (22), we study the effect of the presence of a refractive index mismatch in the intensity distribution in the focal region.
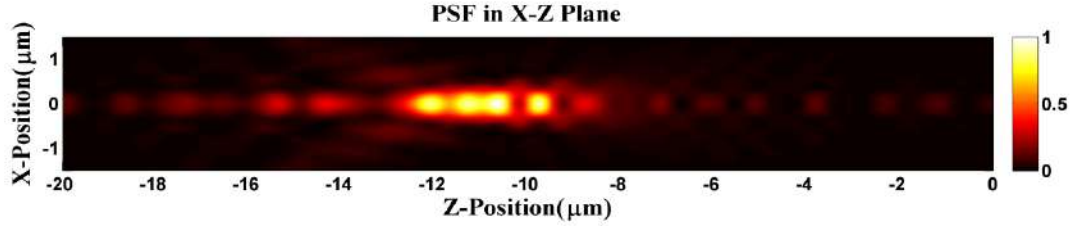

Fig 23. Intensity distribution pattern in the longitudinal plane (X-Z). The input is a Gaussian beam with x-linear polarization. Due to the presence of aberration in the propagation path, the focal region shifts. The new focal region is before the focal point when the medium is homogeneous.
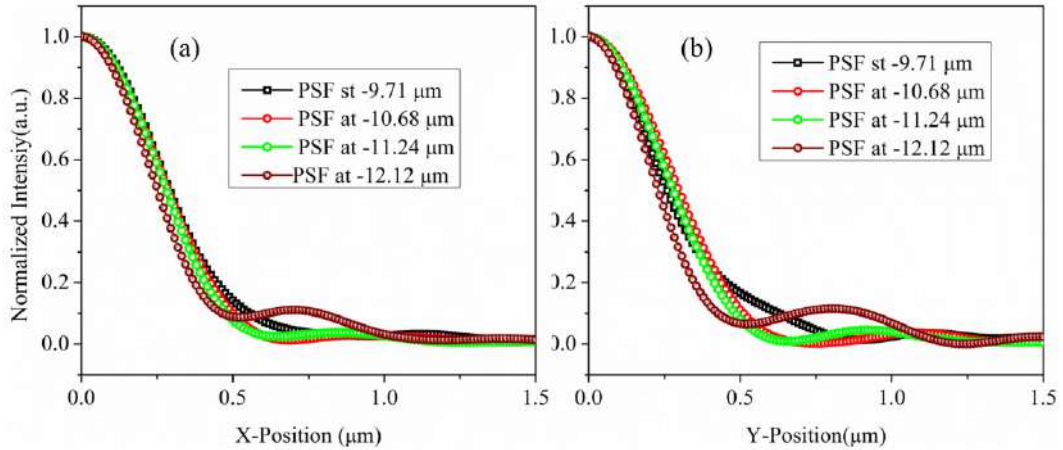

Fig 24. Normalized PSF at the different intense points in the beam propagation path due to presence of stratified media. (a) PSF in the X-direction and (b) PSF in the Y-direction. It is quite clear that spatial resolution in the propagation path has different values.

For our numerical calculations, we have used a 1.4 NA optical lens (oil immersion) objective. The input beam is a Gaussian beam $(exp(-\beta^2)$, $\beta = \sin(\theta_1)/\sin(\alpha))$ with 800 nm wavelength. The beam is taken to be an x-polarized beam. The mismatched mediums are a glass cover-slide and water. The refractive indices are 1.515 and 1.33, respectively. For a typical measurement, d (as shown in Fig 22) is taken to be approximately 80μm.

The results of the numerical simulation for the intensity distribution in the longitudinal path is shown in Fig 23. Not only does the focal point shift ~10 μm from the actual geometrical focal point, the intensity distribution is also split into four major parts. The maxima of these split intensity distributions are at −9.71μm, −10.68μm, −11.24μm and, −12.12μm. The most intense region is at −10.68μm. We note that the FWHM of these intense regions has different values (Fig 24). The FWHM values of the X-coordinate PSFs are 0.57μm, 0.55μm, 0.53μm, and 0.48μm, respectively. The FWHM values of the Y-coordinate PSFs are 0.54μm, 0.57μm, 0.53μm, and 0.43μm, respectively. These values are higher than the values obtained without the presence of a stratified medium (0.365μm and 0.285μm). Thus, we note that the presence of a stratified medium not only reduces the spatial resolution but also creates regions of intensity distribution of different resolutions. Such theoretical observations could also justify our experimentally observed asymmetric intensity distribution in optical tweezers for single and mixed solvents [27].

9 Conclusion

We have numerically studied and investigated the intensity distribution of a focusing spot under tight focusing conditions. With a high NA optical lens, the influence of the incident beam polarization on the intensity distribution of focusing spot is very significant. A linearly polarized incident beam induces an asymmetric focusing spot, which is elongated along the incident beam polarization direction. The incident beam profile influences the shape of the focusing spot. We show that the introduction of an optical mask in front of the optical lens can induce numerous interesting results: Incident beam modulated by an amplitude mask induces a sub-diffraction limit focusing spot; Light beam combined with BPZP masks, possesses a longitudinal doughnut distribution in the focal region and several focal spots in the propagation axis, which are very useful for the study of optical tweezers. We also show that a refractive index mismatch causes a focal point shift in the focal region of the optical lens. Due to the induced spherical aberration, the focusing spot quality is degraded. We have presented numerical studies coupled with relevant experiments to demonstrate and elucidate the variety of effects, which arise during the study of tight-focusing conditions.

Acknowledgments

References

1. Born M, Wolf E, Principles of optics: electromagnetic theory of propagation, interference, and diffraction of light, 7th edn, (Cambridge University Press), 1999.

2. Hecht E, Optics, (Pearson education, Addison-Wesley), 2002.

3. Gu M, Advanced optical imaging theory, *Springer Series in Optical Sciences*, 75(1999)1-214.

4. Wolf E, Electromagnetic diffraction in optical systems I. An integral representation of the image field, *Proceedings of the Royal Society of London. Series A. Mathematical and Physical Sciences*, 253(1959)349-357.

5. Richards B, Wolf E, Electromagnetic diffraction in optical systems. II. structure of the image field in an aplanatic system, *Proceedings of the Royal Society of London. Series A. Mathematical and Physical Sciences*, 253(1959) 358-371.

6. Youngworth K S, Brown T G, Focusing of high numerical aperture cylindrical-vector beams, *Opt Express*, 7(2000)77-87.

7. Foreman M R, Török P, Computational methods in vectorial imaging, *J Mod Opt*, 58(2011)339-364.

8. Rohrbach A, Stiffness of Optical Traps: Quantitative Agreement between Experiment and Electromagnetic Theory, *Phys Rev Lett*, 95(2005)168102; doi.org/10.1103/PhysRevLett.95.168102.

9. Hell S, Stelzer E H K, Properties of a 4pi confocal fluorescence microscope, *J Opt Soc Am A*, 9(1992)2159-2166.

10. Sheppard C J R, Wilson T, Gaussian-beam theory of lenses with annular aperture, *IEE Journal on Microwaves Optics and Acoustics*, 2(1978)105-112.

11. Wang H, Shi L, Lukyanchuk B, Sheppard C, Chong C T, Creation of a needle of longitudinally polarized light in vacuum using binary optics, *Nat Photon*, 2(2008)501-505.

12. Kozawa Y, Sato S, Focusing property of a double-ring-shaped radially polarized beam, *Opt Lett*, 31(2006)820-822.

13. Kuga T, Torii Y, Shiokawa N, HiranoT, ShimizuY, Sasada H, Novel optical trap of atoms with a doughnut beam, *Phys Rev Lett*, 78(1997)4713-4716.

14. Liu T, Tan J, Liu J, Tighter focusing of amplitude-modulated radially polarized vector beams in ultra-high numerical aperture lens systems, *Opt Commun*, 294(2013)21-23.

15. Khonina S N, Simple phase optical elements for narrowing of a focal spot in high-numerical-aperture conditions, *Opt Eng*, 52(2013)091711; doi.org/10.1117/1.OE.52.9.091711.

16. Sheppard C J R, Choudhury A, Annular pupils, radial polarization, and superresolution, *Appl Opt*, 43(2004)4322-4327.

17. Patton B R, Burke D, Vrees R, Booth M J, Is phase-mask alignment aberrating your STED microscope?, *Methods Appl Fluoresce*, 3(2015)024002; doi:10.1088/2050-6120/3/2/024002.

18. Guo H, Weng X, Jiang M, Zhao Y, Sui G, Hu Q, Wang Y, Zhuang S, Tight focusing of a higher-order radially polarized beam transmitting through multi-zone binary phase pupil filters, *Opt Express*, 21(2013)5363-5372.

19. Bokor N, Davidson N, Generation of a hollow dark spherical spot by 4-pi focusing of a radially polarized Laguerre-Gaussian beam, *Opt Lett*, 31(2006)149-151.

20. Sales T R M, Morris G M, Axial superresolution with phase-only pupil filters, *Opt Commun*, 156(1998)227-230.

21. Jabbour T G, Kuebler S M, Vector diffraction analysis of high numerical aperture focused beams modified by two- and three-zone annular multi-phase plates, *Opt Express*, 14(2006)1033-1043.

22. Huang Z, Hao Z, Zhu L, Axial multifocal binary-phase zone plate for high numerical aperture focusing, *Opt Eng*, 55(2016)123101; doi.org/10.1117/1.OE.55.12.123101.

23. Gould T J, Burke D, Bewersdorf J, Booth M J, Adaptive optics enables 3d STED microscopy in aberrating specimens, *Opt Express*, 20(2012)20998-21009.

24. Murray J M, Wei J, Barnes J O, Slagle J E, Guha S, Measuring refractive index using the focal displacement method, *Appl Opt*, 53(2014)3748-3752.

25. Török P, Varga P, Laczik Z, Booker G R, Electromagnetic diffraction of light focused through a planar interface between materials of mismatched refractive indices: an integral representation, *J Opt Soc Am A*, 12(1995)325-332.

26. Török P, Varga P, Konkol A, Booker G R, Electromagnetic diffraction of light focused through a planar interface between materials of mismatched refractive indices: structure of the electromagnetic field II, *J Opt Soc Am A*, 13(1996)2232-2238.

27. Mondal D, Dinda S, Bandyopadhyay S N, Goswami D, Polarization induced control of optical trap potentials in binary liquids, *Sci Rep*, 9(2019)700; doi.10.1038/s41598-018-36856-5.

Debabrata Goswami is presently the Prof S Sampath Chair Professor in the Department of Chemistry, Indian Institute of Technology Kanpur (IITK). He received his Ph D from Princeton University, NJ (USA) in 1994. In the subsequent year, he was a Postdoctoral Fellow at Harvard University, MA (USA). He then held a Research Associateship at the Brookhaven National Labs, New York (USA) during 1995-1996. In 1998, he returned to India as a Faculty member of TIFR, Mumbai, where he stayed for five years. In 2003, he moved to IIT Kanpur, Department of Chemistry, as an Associate Professor and in 2010 was promoted to Professor. He has been invited to several reputed Institutes worldwide as a visiting Professor including MIT, Duke University, IIT Bombay, IMSc. Chennai amongst others. Prof Goswami works at the frontiers of interdisciplinary research involving theoretical and experimental developments investigating the fundamental aspects of femtosecond laser-matter interactions. In the last decade, he has independently carried out research that has included constructing novel experimental equipment. He has made important contributions to the theory of quantum computing, and has uncovered new insights from the consideration of the theoretical aspects of thermal lens generation and analysis. His research has been recognized by the conferment of several academic and research accolades, some of which are the Hoechst Advanced Technology Division Industrial Affiliates Fellowship for outstanding academic record in Princeton, the International Senior Research Fellowship award of the Wellcome Trust (UK), the Swarnajayanti Fellowship of the Department of Science and Technology (Govt. of India), Thathachary Science Award (India). He is a Fellow of the Royal Society of Chemistry, the Institute of Physics, the Optical Society of America, and the Society of Photo-Optical Instrumentation Engineers (SPIE). He is a Senior Member of IEEE and URSI. His work in ultrafast optics and light-matter interactions has also been recognized by the 2019 Galileo Galilei award of the International Commission of Optics. He has published over two hundred research articles, several book chapters, edited conference proceedings and books. He is on the Editorial Board of several journals including Science Advances, Peer J, PLOS ONE, and has been the Editor-in-charge of Journal of Spectroscopy and Dynamics. His research has been supported by grants and funds by many branches of the Indian Government, including the Ministry of Electronics and Information Technology (MEITY), the Ministry of Science and Technology (DST), the Indian Space Research Organization Space Technology Cell (ISRO-STC) as well as international collaborations and fellowships.

Dr Sirshendu Dinda is currently a post-doctoral researcher at the Helmholtz Institute Ulm, Germany, where he is working on the Tip Enhanced Raman Spectroscopy (TERS) and Raman chemical imaging of electrochemical interface. He finished his M Sc as well as Ph D program (CSIR fellow) from IIT Kanpur with scholarship. In Ph D he has worked on femtosecond optical pulse shaping, optical tweezers, nonlinear spectroscopy and microscopy, etc. He has developed a unique technique which can generate Megahertz shaped optical pulse train using acousto optic modulator, which was incomprehensible previously. After finishing his Ph D, he joined S N Bose National Centre for Basic Sciences, Kolkata as a post-doctoral researcher, where he worked on ultrafast solvation and reaction dynamics of photo active molecules in complex condensed medium which imitates glassy or supercooled liquid properties.